analytical chemistry

pubs.acs.org/ac Article

Versatile Photoelectrochemical Biosensing for Hg^{2+} and Aflatoxin B1 Based on Enhanced Photocurrent of $AgInS_2$ Quantum Dot−DNA Nanowires Sensitizing NPC−ZnO Nanopolyhedra

Qianqian Cai, Tengyue Yin, Yuhang Ye, Guifen Jie,* and Hong Zhou

Cite This: *Anal. Chem.* 2022, 94, 5814−5822 Read Online

ACCESS | Metrics & More | Article Recommendations | Supporting Information

ABSTRACT: Eliminating false positives or negatives in analysis has been a challenge. Herein, a phenomenon of polarity-switching photocurrent of $AgInS_2$ quantum dot (QD)−DNA nanowires reversing nitrogen-doped porous carbon−ZnO (NPC−ZnO) nanopolyhedra was found for the first time, and a versatile photoelectrochemical (PEC) biosensor with a reversed signal was innovatively proposed for dual-target detection. NPC−ZnO is a photoactive material with excellent PEC properties, while $AgInS_2$ QDs as a photosensitive material match NPC−ZnO in the energy level, which not only promotes the transfer of photogenerated carriers but also switches the direction of PEC current. Furthermore, in order to prevent spontaneous agglomeration of $AgInS_2$ (AIS) QDs and improve its utilization rate, a new multiple-branched DNA nanowire was specially designed to assemble $AgInS_2$ QDs for constructing amplified signal probes, which not only greatly increased the load of $AgInS_2$ QDs but also further enhanced the photoelectric signal. When the target Hg^{2+}-induced cyclic amplification process generated abundant RDNA, the DNA nanowire signal probe with plenty of QDs was linked to the NPC−ZnO/electrode by RDNA, generating greatly amplified polarity-reversed photocurrent for signal "ON" detection of Hg^{2+}. After specific binding of the target (aflatoxin B1, AFB1) to its aptamer, the signal probes of AIS QD-DNA nanowires were released, realizing signal "OFF" assay of AFB1. Thus, the proposed new PEC biosensor provides a versatile method for detection of dual targets and also effectively avoids both false positive and negative phenomena in the assay process, which has great practical application potential in both environmental and food analysis.

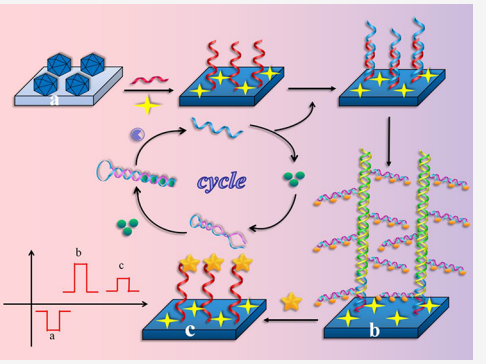

Food safety has become a hot issue of concern. Industrial sewage containing mercury pollutes fish, shrimp, and shellfish in lake and river water. The pesticides containing mercury also directly pollute plant food raw materials,[1,2] and these foods can cause great harm at very low concentrations.[3] In addition, many agricultural products may be contaminated by aflatoxin B1 (AFB1) due to the unrestricted growth of fungi, which can bind to DNA of living organisms and increase the risk of human cancer complications.[4,5] Therefore, it is essential to develop sensitive and reliable analytical methods for the timely detection of the trace Hg^{2+} and AFB1 content. The current methods for detecting Hg^{2+} and AFB1 mainly include atomic absorption/emission spectrometry,[6] redox potential determination,[7] chromatography,[8] and enzyme-linked immunosorbent assay.[9] Despite their high accuracy and selectivity, these methods have high costs, long sample pretreatment time, and high equipment precision requirements.[10]

Photoelectrochemical (PEC) biosensors can convert biochemical indicators into readable photocurrent *via* transfer of electrons and holes between photosensitive materials and electrodes, which has higher sensitivity and reduced background than traditional electrochemical and optical methods.[11] This technology has been widely used in various kinds of detections and analyses due to its low cost, simple detection process, and easy miniaturization.[12] However, these sensors analyze the increase or decrease in the PEC signal relative to the background, without changing the direction of photocurrent, and cannot avoid false positive or negative signals from other redox substances and biological molecules. In order to fundamentally avoid above-mentioned problems, target-induced photocurrent direction switching may be a promising method for PEC sensors.[13] The metal−organic frameworks (MOFs) are widely used in photochemical analysis because of their high specific surface area and high porosity, which are favorable for photoelectron transport.[14,15] NPC−ZnO nanopolyhedra derived from ZIF-8 are a direct band gap p-type semiconductor with larger surface area, more porous structure, and higher electrical conductivity.[16] Moreover, terpolymer I-

Received: December 5, 2021
Accepted: March 24, 2022
Published: April 5, 2022

https://doi.org/10.1021/acs.analchem.1c05250
Anal. Chem. 2022, 94, 5814−5822

Scheme 1. (A) Schematic Diagram for Versatile Photoelectrochemical Biosensing of Hg^{2+} and Aflatoxin B1 Based on Enhanced Photocurrent of $AgInS_2$ QD−DNA Nanowires Sensitizing NPC−ZnO Nano-polyhedron and (B) Preparation of $AgInS_2$ QD−DNA Nanowires

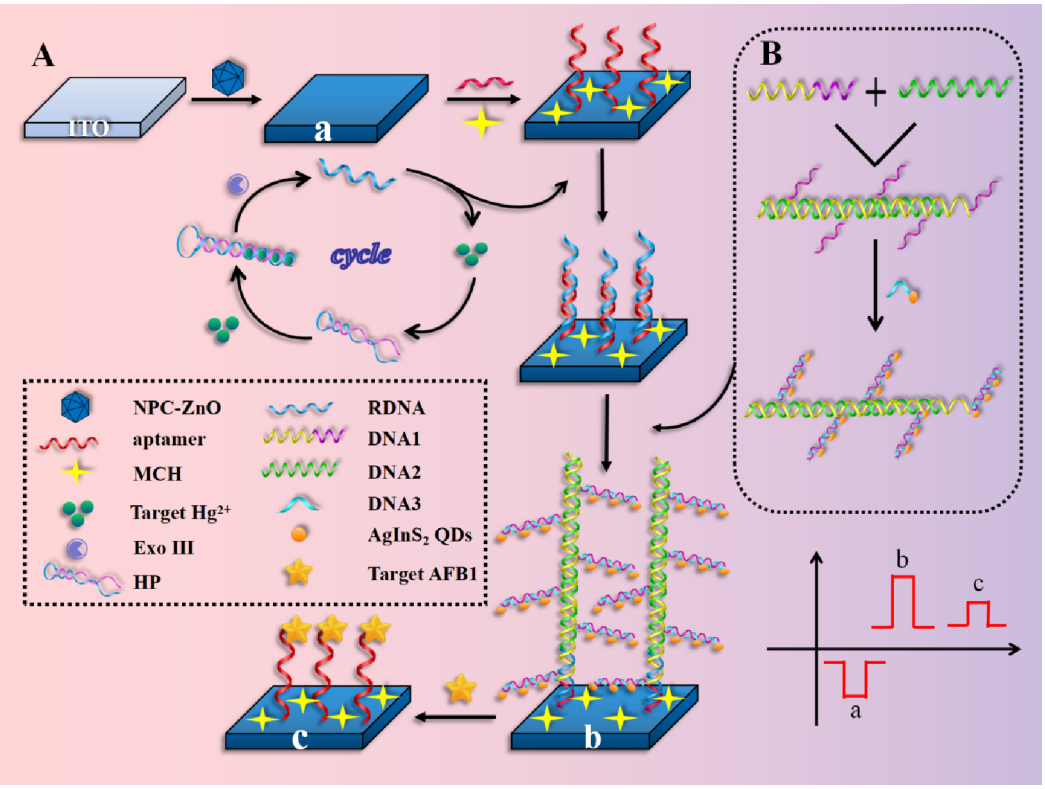

III-VI2 $AgInS_2$ (AIS) QDs have the advantages of low toxicity, high photoelectroactivity, and an adjustable band gap.[17−19] More importantly, $AgInS_2$ QDs have a well-matched band-edge energy level with the NPC−ZnO, which can generate a reversed photocurrent signal, thus avoiding false positive or negative signals.

However, QDs tend to spontaneously agglutinate and reduce their utilization rate. To solve this problem, the researchers have developed a variety of DNA nanostructures to load abundant QDs for fabricating amplified signal probes, thus much improving their utilization rate.[20,21] In our previous work, CdSe QDs were assembled onto electrodes via a 3D DNA nanonetwork to improve CdSe utilization.[22]

In this work, the unique DNA nanowires were assembled to load AIS QDs to construct amplified signal probes. DNA nanowires were easily connected to electrodes, which not only increased the loading capacity of AIS QDs but also further improved the photocurrent signal. Therefore, a versatile PEC biosensor was designed to detect dual targets (Hg^{2+} and AFB1) based on polarity-switching photocurrent of $AgInS_2$ QD−DNA nanowires reversing NPC−ZnO nanopolyhedra.

In Scheme 1A, the amino-functionalized NPC−ZnO polyhedra were first modified on the electrode and showed cathodic photocurrent. Then, the AFB1 aptamer was connected to the electrode by an amide bond. Meanwhile, Hg^{2+} induces the cyclic amplification process (cycle) to generate a large amount of RDNA, which binds to the AFB1 aptamers on the electrode. In Scheme 1B, the DNA nanowires were formed by hybridization of DNA1 with DNA2, and then, DNA3 labeled with AIS QDs hybridized with DNA1 to form the AIS QD−DNA nanowire signal probes. Then, the signal probes were modified onto the electrode by RDNA, thus generating extremely strong anodic photocurrent for sensitive detection of Hg^{2+}. Subsequently, target AFB1 specifically binds to its aptamer, so AIS QD−DNA nanowires are replaced from the electrode, achieving the "off" photocurrent signal for sensitive detection of AFB1.

EXPERIMENTAL SECTION

Preparation of $AgInS_2$ QD−DNA Nanowires. The mixture of 50 μL of DNA1 (1 μM) and 50 μL of DNA2 (1 μM) was heated at 95 °C for 5 min and cooled naturally to obtain the hybrid product of DNA1 and DNA2.

The prepared $AgInS_2$ QDs were washed with anhydrous ethanol and centrifuged (5000 rpm, 5 min) three times and then re-dispersed in equal volume of water. 70 μL of $AgInS_2$ QDs was purified, and 15 μL of EDC/NHS solution (0.1 M EDC and 0.025 M NHS) was added to the mixture for 40 min, and then, 15 μL of DNA3 (10 μM) was added to it. The mixture was put into a shaker at 37 °C for 6 h to get the $AgInS_2$ QD−DNA3 conjugate. Then, $AgInS_2$ QD−DNA3 was centrifuged again and dispersed in water.

Then, the hybridization products of DNA1 and DNA2 were added to the mixed solution of $AgInS_2$ QD−DNA3 and incubated for 2 h. The DNA nanowire−$AgInS_2$ QD probe was obtained by centrifugation.

Target Hg^{2+}-Induced Amplification Process. 30 μL of HP (5 μM), 6 U Exo III, and 30 μL of different concentrations of Hg^{2+} solutions were added to 40 μL of Tris−HCl buffer, reacting at 37 °C for 150 min to prepare RDNA. Then, it was heated to 80 °C for 10 min and cooled naturally. Finally, RDNA was stored at 4 °C.

https://doi.org/10.1021/acs.analchem.1c05250
Anal. Chem. 2022, 94, 5814−5822

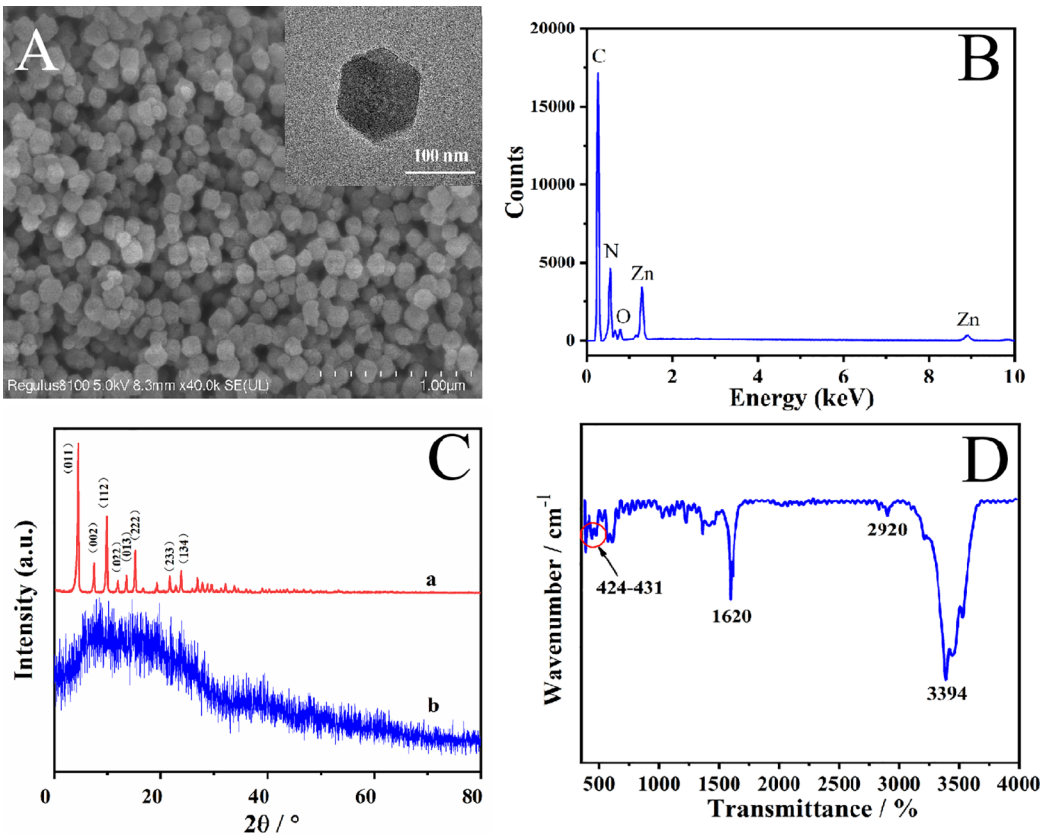

Figure 1. (A) SEM image of NPC−ZnO (inset: the TEM image of NPC−ZnO), (B) EDS spectra of NPC−ZnO, (C) XRD spectra of NPC−ZnO, and (D) FTIR spectra of aminated NPC−ZnO.

Preparation of the PEC Sensing Platform. The AFB1 aptamer was activated with the 10 mM EDC/NHS mixture. 20 μL of 0.5 mg mL^{-1} aminoated NPC−ZnO was dropped onto the ITO electrode. After drying, 20 μL of the activated AFB1 aptamer was added and incubated at 37 °C for 2 h, and then, the modified electrode was blocked with 1 mM mercaptohexanol (MCH) for 1 h. Next, RDNA at various concentrations was connected with the AFB1 aptamer at 37 °C for 2 h. Next, 20 μL of DNA nanowires−$AgInS_2$ QDs was added and reacted for 2 h, constructing the PEC sensing platform for detecting Hg^{2+}. After each step of incubation on the electrode, the platform was slightly rinsed with ultra-pure water to remove the unconnected reactants. The completed PEC sensing platform was dried in air for testing.

Next, standard solutions of AFB1 in different concentrations were prepared with PBS (0.1 M, pH = 7.0). After the above-mentioned electrodes responding to a fixed concentration of Hg^{2+} were completed, they were incubated with AFB1 solutions at different concentrations for 2 h, rinsed with PBS, and dried in air for AFB1 assay.

Extraction of AFB1 From Peanut Samples. To extract AFB1 from moldy food samples, peanuts were first pretreated: clean peanuts were shredded with a knife and stored in a humid environment at 37 °C for 7 days.[23] 1 g of the peanut sample was added to 2 mL of methanol and shaken well for 1 h. After centrifuging three times, the extracted solution was transferred to the same centrifuge tube. Finally, the sample was extracted in 100 μL of solution for electrochemical detection.

RESULTS AND DISCUSSION

Morphology, Structure, and Properties of NPC−ZnO. Scanning electron microscopy (SEM) images (Figure 1A) showed that the NPC−ZnO had a typical rhomboid dodecahedron structure and good morphology, which was consistent with previous reports.[24] The inset shows a transmission electron microscopy (TEM) image of an NPC−ZnO polyhedron. The average diameter of an NPC−ZnO polyhedron is about 100 nm. The elemental composition of the NPC−ZnO nanopolyhedron was analyzed by energy-dispersive X-ray spectroscopy (EDS) (Figure 1B). As shown in the figure, the NPC−ZnO nanopolyhedron has four elements (C, N, O, and Zn), which are evenly distributed. In Figure 1C, the X-ray diffraction (XRD) of the ZIF-8 polyhedron (curve a) is well matched with the previously reported XRD pattern.[25] However, in the XRD pattern of NPC−ZnO (curve b), the typical peak of ZIF-8 disappeared, indicating that the crystal structure of ZIF-8 was completely destroyed when heated to 600 °C, and the Zn element in ZIF-8 was transformed into ZnO after heating, which was confirmed by EDS results (Figure 1B).

Figure 1D shows the Fourier transform infrared spectra of NPC−ZnO after amination. The sample shows the characteristic absorption peak of the Zn−O bond at 424−431, and 1620 cm^{-1} is the flexural vibration stretching peak of the O−H bond. 2920 cm^{-1} is attributed to the C−H stretching vibration peak, and the sharp peak at 3394 cm^{-1} is the N−H stretching vibration peak of the secondary amine.

In addition, NPC−ZnO was analyzed by X-ray photoelectron spectroscopy (XPS). Figure S1A shows that NPC−ZnO contains Zn, C, N, O elements, which is also confirmed

https://doi.org/10.1021/acs.analchem.1c05250
Anal. Chem. 2022, 94, 5814−5822

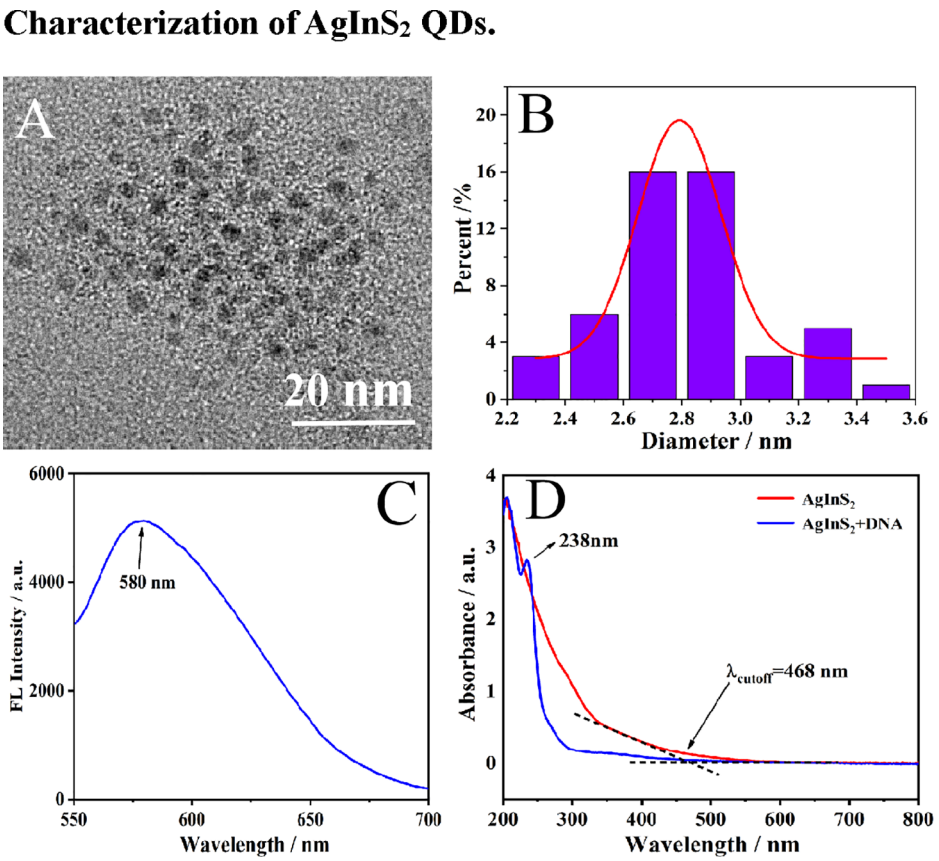

Figure 2. (A) TEM image of AIS QDs, (B) size distribution of AIS QDs, (C) PL emission spectra of AIS QDs, and (D) UV−vis absorption of AIS QDs.

by EDS (Figure 1B). Figure S1B shows the high-resolution XPS of C 1s. The peak at 282.6 eV is attributed to the binding energy of the C sp^3 orbital.[26] The NPC−ZnO nanopolyhedron has a peak at 396.5 eV in the N 1s spectrum (Figure S1C), which is attributed to pyridine nitrogen.[27] The presence of lone electron pairs promotes electron transfer, providing additional advantages for PEC biosensors. The two peaks at 1019.5 and 1042.4 eV belong to Zn $2p_{3/2}$ and $2p_{1/2}$, respectively, and constitute the Zn 2p spectrum of NPC−ZnO nanopolyhedra (Figure S1D), which also proves that Zn^{2+} exists in NPC−ZnO nanopolyhedra. The results show that NPC−ZnO nanopolyhedrons are N-doped carbon−zinc oxide composites.

Characterization of $AgInS_2$ QDs. Figure 2A shows the TEM image of water-soluble AIS QDs, which are evenly distributed and uniform in size. According to the particle size distribution in Figure 2B, the average diameter of QDs is 2.8 ± 0.2 nm. Figure 2C is the fluorescence spectrum of AIS QDs, and the emission peak is at 580 nm. Figure 2D shows the UV−vis absorption spectrum of AIS QDs, whose absorption range is wide to below 468 nm. There is no obvious exciton peak in the absorption of AIS QDs, and the peak comes from the defect position in the gap band.[28] When DNA3 was connected to the AIS QDs, the DNA peak was at 238 nm, which showed a blue shift compared to that at 260 nm, indicating that AIS QD-labeled DNA3 was successfully formed.

PAGE Characterization. The sensing process of DNA on the electrode surface was studied through polyacrylamide gel electrophoresis (PAGE) analysis. As shown in Figure 3A, the leftmost lane is the marker, and lanes 1, 2, and 3 are RDNA, the AFB1 aptamer, and DNA1, respectively. As expected, a new band appeared in lane 4, and the AFB1 aptamer and RDNA at the original location disappeared, indicating that the AFB1 aptamer effectively hybridized with RDNA, so RDNA can attach to the electrode by hybridization. Similarly, the new band in lane 5 shows that RDNA can efficiently hybridize with DNA1, thus connecting DNA1 to the electrode surface. In lane 6, the new band further confirms that the AFB1 aptamer, RDNA, and DNA1 can hybridize with each other; thus, the DNA1-linked probe can be connected to the electrode.

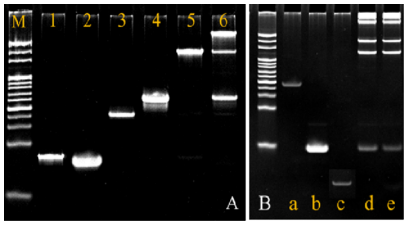

Figure 3. (A) PAGE analysis of the sensing process: lane 1: RDNA, lane 2: AFB1 aptamer, lane 3: DNA1, lane 4: AFB1 aptamer + RDNA, lane 5: RDNA + DNA1, and lane 6: AFB1 aptamer + RDNA + DNA1. (B) PAGE analysis of DNA nanowire construction: lane a: DNA1, lane b: DNA2, lane c: DNA3, lane d: DNA1 + DNA2, and lane e: DNA1 + DNA2 + DNA3.

Figure 3B shows the formation process of DNA nanowires. Lanes a, b, and c are DNA1, DNA2, and DNA3, respectively. In lane d, the new bands were obvious, indicating that the DNA nanowires with different lengths were formed by cross-hybridization of DNA1 and DNA2. In lane e, after DNA3 was

https://doi.org/10.1021/acs.analchem.1c05250
Anal. Chem. 2022, 94, 5814−5822

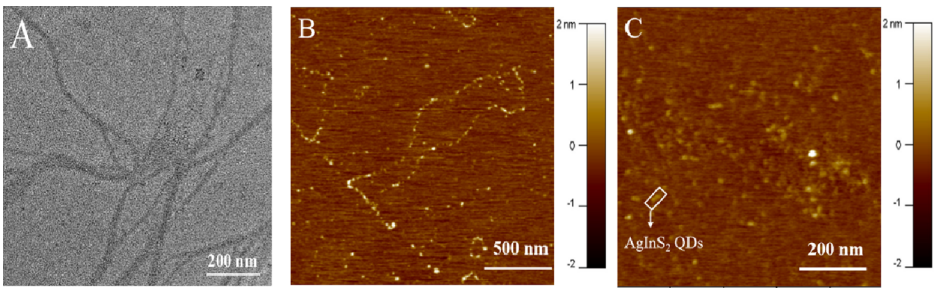

Figure 4. TEM (A) and AFM (B) of the DNA nanowires. (C) AFM image of AIS QD−DNA nanowires.

added, the base number of DNA3 was far less than that of DNA1 and DNA2, so there was no significant difference between DNA3 and the new bands generated in lane d. The disappearance of DNA3 in the original location indicated that DNA3 was fully hybridized, which could prove the successful synthesis of DNA nanowires.

Characterization of $AgInS_2$ QD−DNA Nanowires. The synthesized DNA nanowires were verified by TEM (Figure 4A) and atomic force microscopy (AFM) (Figure 4B) images. Figure 4A shows the DNA nanowires with uniform dispersion and high yield. The theoretical width of DNA is 2.2−2.6 nm.[29] However, the DNA nanowires in this work not only contain the hybridized DNA part but also have several unhybridized DNA sequences at the end of DNA1. As a result, this may cause DNA nanowires to intercross,[30] allowing multiple strands of nanowires to form bundles and may increase the width of DNA nanowires.[30] It is also worth noting that the width of DNA nanowires in the reported AFM and TEM images is consistent with our results.[31,32] It can be seen from Figure 4B that the average length of the nanowire is 800 nm ± 100 nm, and the height is 2 nm, which is consistent with the length of the nanowire in the TEM image. In order to verify the successful formation of AIS QD−DNA nanowires, AFM image analysis was carried out (Figure 4C). The large number of yellow spots found in the figure is consistent with $AgInS_2$ QD size (Figure 2A), which proves that $AgInS_2$ QDs successfully labeled DNA nanowires.

PEC Reaction Mechanism. Band calculations for semiconductors are in the Supporting Information (Figure S2). As shown in Scheme 2A, when visible light excited, electrons (e^-) in the NPC−ZnO valence band (VB) transition to the conduction band (CB), thus forming photogenic holes (h^+) in the VB, while electrons (e^-) in the CB are absorbed by dissolved O_2. The electrons (e^-) in the ITO electrode transfer to the hole (h^+) in the NPC−ZnO valence band, and the presence of AA also provides electrons (e^-) to the NPC−ZnO VB, and the electrons (e^-) constantly transfer to the CB, thus generating cathode photocurrent. In Scheme 2B, the VB position (−2.17 eV) and CB position (−4.82 eV) of AIS QDs are higher than those of NPC−ZnO (−0.55 and −3.78 eV), respectively. When visible light excited, the excited electrons (e^-) transfer from the VB of AIS QDs to the CB and then transfer to the CB of NPC−ZnO, while the photogenerated hole (h^+) in NPC−ZnO migrates from the VB of NPC−ZnO to the VB of AIS QDs. At the same time, due to the existence of AA, the photo-generated holes (h^+) in the VB of AIS QDs are continuously consumed, which promotes separating electron−hole pairs and improves photoelectric conversion efficiency. Finally, the excited electrons (e^-) in the conduction band of NPC−ZnO are transferred to the electrode to generate anodic photocurrent.

Scheme 2. (A) Possible Electron-Transfer Mechanisms of NPC−ZnO and (B) Reaction Mechanism of NPC−ZnO with AIS QDs

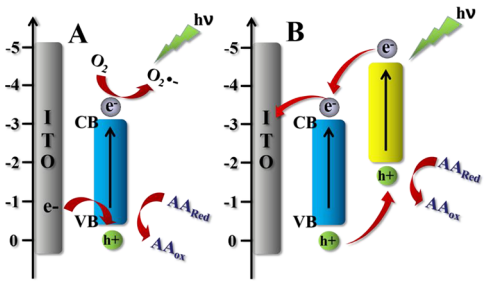

Characterization of the Biosensor Manufacturing Process. SEM can be used to confirm the assembly process of the biosensor. Figure S3A shows the image of the NPC−ZnO polyhedron on the ITO electrode, and the uniform particle size is consistent with that of NPC−ZnO (Figure 1A). When the target Hg^{2+} is present, the RDNA produced by the cyclic amplification process linked the AIS QD−DNA nanowires to the electrode, and the electrode surface became denser and more dispersed (Figure S3B). When target AFB1 appeared, it would specifically bound with the AFB1 aptamer on the electrode surface, replacing the AIS QD−DNA nanowires. The aggregates of the AFB1-aptamer conjugate were formed on the electrode surface (Figure S3C), indicating that the biosensor was successfully constructed based on NPC−ZnO polyhedra and AIS QD−DNA nanowires, which can be used for dual-target detection.

Feasibility of the Biosensor for Hg^{2+} and AFB1. Figure 5A displays the PEC signals of different modification electrodes. The bare electrode shows a negligible PEC signal (curve a). When NPC−ZnO drops onto the electrode, the cathode photocurrent is about 100 nA (curve b). In the absence of target Hg^{2+}, due to the steric hindrance of DNA, the impedance increased, and the signal decreased slightly (curve c). However, in the presence of target Hg^{2+}, the RDNA was generated by cyclic amplification, and then, the AIS QD−DNA nanowires as signal probes were connected to the electrode, reversing the photocurrent signal to 3.4 μA (curve d), which proved that the QD nanowire-based PEC sensor for Hg^{2+} was successfully fabricated.

Figure 5B shows the photocurrent signal continuously for 200 s, and RSD is 1.65%, showing good stability. Figure 5C studies the feasibility of detecting target AFB1. The PEC signal of bare ITO is negligible (curve a), and the background signal without target AFB1 is about 3.4 μA (curve b). When AFB1

https://doi.org/10.1021/acs.analchem.1c05250
Anal. Chem. 2022, 94, 5814−5822

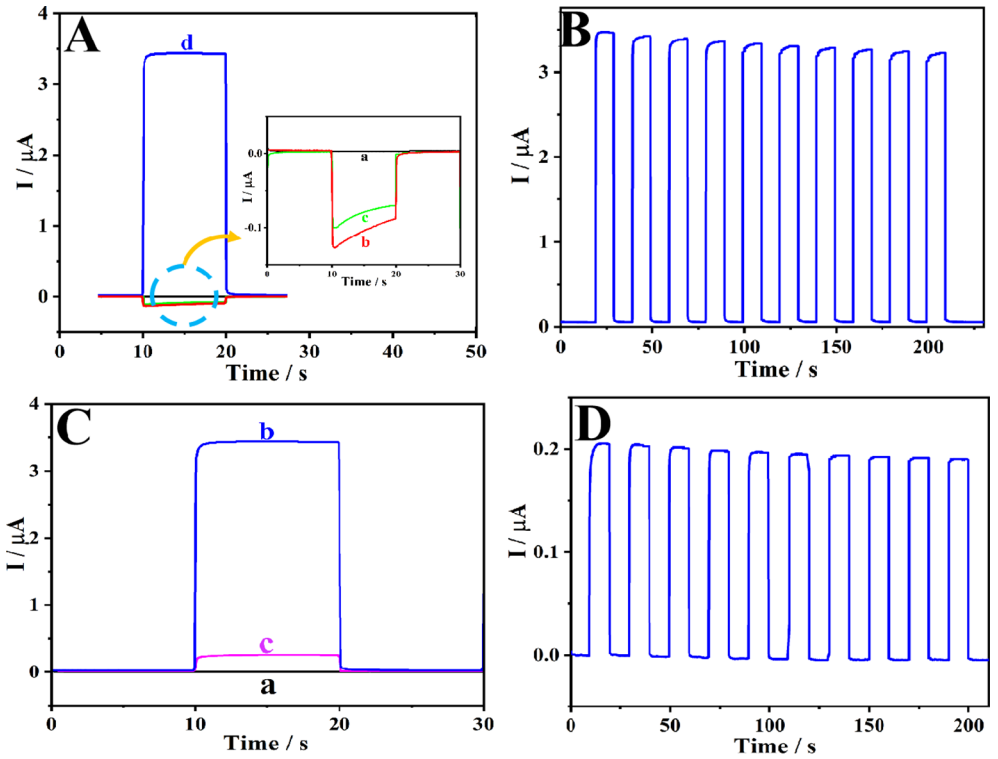

Figure 5. (A) Photocurrent responses of different modification electrodes: (a) bare electrode, (b) electrode/NPC−ZnO, (c) electrode/NPC−ZnO/AFB1 aptamer/AIS QD−DNA nanowires (without Hg^{2+}), and (d) electrode/NPC−ZnO/AFB1 aptamer/RDNA/AIS QD−DNA nanowires (with Hg^{2+}); (B) stability of the sensor for detecting Hg^{2+} for 200 s (Hg^{2+}: 0.1 μM); (C) PEC responses of different modification electrodes: (a) bare electrode, (b) electrode/NPC−ZnO/AFB1 aptamer/RDNA/AIS QD−DNA nanowires (Hg^{2+}: 0.1 μM), and (c) electrode/NPC−ZnO/AFB1 aptamer/RDNA/AIS QD−DNA nanowires/AFB1; and (D) stability of the sensor for detecting AFB1 by continuous scanning for 200 s (AFB1: 10 ng mL^{-1}).

was present, the AIS QD−DNA nanowires were replaced due to the specific binding of AFB1 to the aptamer; thus, the anodic photocurrent decreased to 0.2 μA (curve c), indicating that the sensor is feasible for the detection of AFB1. In Figure 5D, when the AFB1 concentration is 10 n mL^{-1}, the photocurrent of the biosensor was 0.2 μA (RSD = 1.12%), and the signal is stable. Therefore, this designed sensor can be used for the detection of Hg^{2+} and AFB1.

Optimization of Experimental Conditions. This section is in the Supporting Information (Figure S4).

Detection of Hg^{2+} and AFB1 Signal by using Biosensor. The PEC responses of the biosensing platform to Hg^{2+} at different concentrations were measured. In the presence of Hg^{2+}, AIS QD−DNA nanowires were captured on the electrode, and we reversed the cathode photocurrent (100 nA) to the anode signal (3.4 μA). Figure 6A shows that the inversion effect of AIS QD−DNA nanowires on NPC−ZnO is related to the concentration of Hg^{2+}. When the concentration of Hg^{2+} increased, the photocurrent signal increased, showing a good linear relationship in the range of 1 fM∼0.1 μM (Figure 6B, $y = 0.4102 \log x + 2.635$), and the limit of detection (LOD) was 0.132 fM (S/N = 3).[33] The sensor showed better sensitivity compared to the reported Hg^{2+} assay (Table S2). According to the above-mentioned results, the designed PEC sensing platform based on the photocurrent inversion and amplification effects of AIS QD−DNA nanowires has excellent detection performance for Hg^{2+} detection.

Under the same conditions, the photocurrent response of the PEC platform to different concentrations of AFB1 was measured. When target AFB1 binds to its aptamer, the AIS QD−DNA nanowires were replaced to reduce the photocurrent, demonstrating that the signal is related to the AFB1 concentration. When the concentration of AFB1 increased, the photocurrent responses decreased (Figure 6C), presenting a good linear relationship in the range of 1 fg mL^{-1} to 10 ng mL^{-1} (Figure 6D, $y = 0.431 \log x + 2.728$). The LOD is 0.608 fg mL^{-1}, much lower than that of previously reported methods (Table S3). According to the above-mentioned results, the biosensor has performed well for AFB1 detection.

Selectivity of the Biosensors for Detecting Hg^{2+} and AFB1. Using 0.1 μM Zn^{2+}, Mg^{2+}, Ca^{2+}, K^{+}, Cu^{2+}, and the mixed solution (containing 0.1 μM Zn^{2+}, Mg^{2+}, Ca^{2+}, K^{+}, Cu^{2+}, and Hg^{2+}) as comparison, the selectivity of the proposed electrochemical sensor for Hg^{2+} detection was studied. It can be clearly seen that the PEC signals' response to target Hg^{2+} is much higher than that to other ions (Figure 7A). Meanwhile, the PEC signal of the mixed sample is close to that of Hg^{2+}, indicating that the sensor has good selectivity for Hg^{2+} detection.

In addition, the selectivity of the biosensor for AFB1 detection was studied by using the same amount of AFB2, AFG1, AFG2, AFM1, and its mixture as the interference substances. As shown in Figure 7B, the PEC signal changes were observed only in the presence of AFB1, and other interfering substances had no significant effect on the PEC signal, which proved that the biosensor had excellent selectivity for AFB1 determination.

Detection of Actual Samples by using Biosensor. In order to evaluate the practical application of the proposed sensing platform in detecting Hg^{2+} in different environmental

https://doi.org/10.1021/acs.analchem.1c05250
Anal. Chem. 2022, 94, 5814−5822

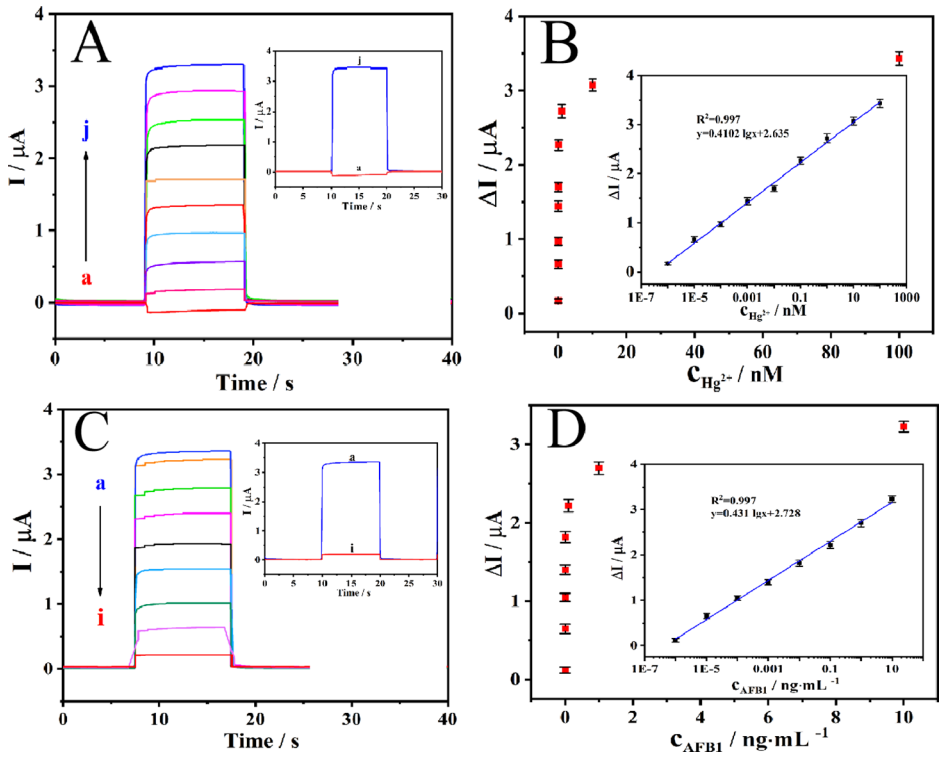

Figure 6. (A) PEC sensor platform responds to different concentrations of Hg^{2+}: 0, 1, 10, 100 fM, 1, 10, 100 pM, 1, 10 nM, and 0.1 μM. (B) Relationship of the PEC signal changes with Hg^{2+} concentrations (1 fM−0.1 μM). (C) Photocurrent curves of the PEC platform for different AFB1 concentrations: 0, 1, 10, 100 fg mL^{-1}, 1, 10, 100 pg mL^{-1}, 1, and 10 ng mL^{-1}. (D) Relationship of the PEC signal changes with AFB1 concentrations. (1 fg mL^{-1}−10 ng mL^{-1}).

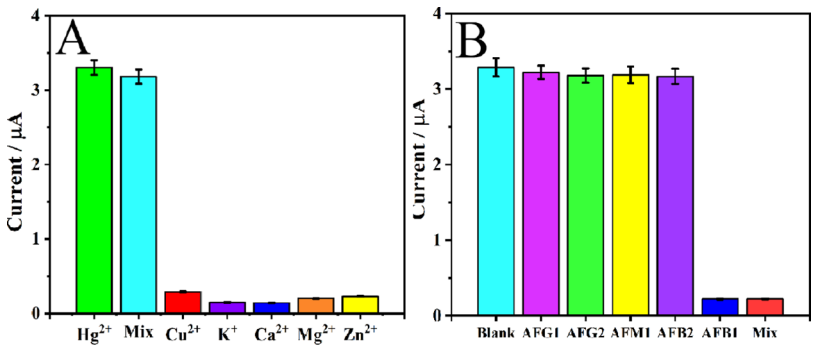

Figure 7. (A) Selectivity of the biosensor for Hg^{2+} (0.1 μM) by comparing with 0.1 μM Zn^{2+}, Mg^{2+}, Ca^{2+}, K^{+}, Cu^{2+}, and the mixed solutions (containing 0.1 μM Zn^{2+}, Mg^{2+}, Ca^{2+}, K^{+}, Cu^{2+}, and Hg^{2+}). (B) Selectivity of the biosensor for AFB1 (10 ng mL^{-1}) by comparing with 10 ng mL^{-1} AFB2, AFG1, AFG2, AFM1, the mixed solution (AFB1/AFB2/AFG1/AFG2/AFM1 = 1:1:1:1: 1), and the blank sample.

water samples, the collected real samples include drinking tap water, purified water, surface water, and high-mineral water. The standard addition method was used to determine Hg^{2+}, and the results are shown in Table S4. In tap water samples, the recovery rate of Hg^{2+} was 96.41−98.22%, and the RSD was 1.26−4.85%. The recoveries of pure water samples were 92.23−103.10% with an RSD of 1.85−3.87%. For surface water samples, the recoveries of Hg^{2+} were 93.83−98.32% with an RSD of 1.07−2.67%. In the high mineral water samples, the recoveries are between 94.20 and 98.74%, and RSD is above 1.88−2.98%, which proves the practicability of our method to detect Hg^{2+} in actual samples.

In order to evaluate the detection of the sensor in actual samples, the clean peanut samples (Figure S5A) and moldy peanut samples (Figure S5B) were added with 0.1, 1, and 10 ng mL^{-1} standard AFB1 for recycling tests. Experimental results showed that the moldy samples originally contained a small amount of AFB1, and the results are shown in Table S5, and the recoveries and RSD of AFB1 were in the range of 94.23−109.42% and 3.08−7.23%, respectively, indicating that the PEC sensor can be used for the actual detection of AFB1.

CONCLUSIONS

In this work, a versatile PEC biosensor based on AIS QD−DNA nanowires reversing the photoelectric signal of NPC−ZnO polyhedra was proposed for dual target detection. The novel porous nano-polyhedron NPC−ZnO has excellent PEC performance under visible light, and $AgInS_2$ QDs as a photosensitive material can not only promote the effective transmission of photogenerated carriers of NPC−ZnO but also reverse the photocurrent signal. Moreover, the assembled AIS

https://doi.org/10.1021/acs.analchem.1c05250
Anal. Chem. 2022, 94, 5814−5822

QD−DNA nanowires with abundant QDs displayed much improved photocurrent and stability, which was combined with Hg^{2+}-induced cyclic amplification to generate an extremely strong anodic PEC signal for sensitive detection of Hg^{2+}. Furthermore, the second target AFB1 can replace AIS QD−DNA nanowires by binding with the aptamer, achieving the photocurrent "off" signal for AFB1 detection. The method proposed a new PEC polarity-switching mechanism of QDs to NPC−ZnO and constructed a novel QD nanowire with a high PEC signal and stability, which were applied to design a versatile biosensor for sensitive, rapid, and accurate "on−off" assay of Hg^{2+} and AFB1. The biosensor was well applied in actual samples with no false positives or negatives in analysis.

■ ASSOCIATED CONTENT

Supporting Information

The Supporting Information is available free of charge at https://pubs.acs.org/doi/10.1021/acs.analchem.1c05250.

Reagents and apparatus, synthesis of NPC−ZnO polyhedra, polyacrylamide gel electrophoresis analysis, XPS of NPC−ZnO, PEC reaction mechanism, characterization of the biosensor manufacturing process, optimization of experimental conditions, comparison of different methods for detecting Hg^{2+} and AFB1, recoveries of Hg^{2+} in different water samples, and recoveries of AFB1 in the actual sample (PDF)

■ AUTHOR INFORMATION

Corresponding Author

Guifen Jie − *Key Laboratory of Optic-electric Sensing and Analytical Chemistry for Life Science, MOE; College of Chemistry and Molecular Engineering, Qingdao University of Science and Technology, Qingdao 266042, PR China;* orcid.org/0000-0002-6416-6523; Email: guifenjie@126.com

Authors

Qianqian Cai − *Key Laboratory of Optic-electric Sensing and Analytical Chemistry for Life Science, MOE; College of Chemistry and Molecular Engineering, Qingdao University of Science and Technology, Qingdao 266042, PR China*

Tengyue Yin − *Key Laboratory of Optic-electric Sensing and Analytical Chemistry for Life Science, MOE; College of Chemistry and Molecular Engineering, Qingdao University of Science and Technology, Qingdao 266042, PR China*

Yuhang Ye − *Key Laboratory of Optic-electric Sensing and Analytical Chemistry for Life Science, MOE; College of Chemistry and Molecular Engineering, Qingdao University of Science and Technology, Qingdao 266042, PR China*

Hong Zhou − *Key Laboratory of Optic-electric Sensing and Analytical Chemistry for Life Science, MOE; College of Chemistry and Molecular Engineering, Qingdao University of Science and Technology, Qingdao 266042, PR China;* orcid.org/0000-0002-9264-7148

Complete contact information is available at: https://pubs.acs.org/10.1021/acs.analchem.1c05250

Notes

The authors declare no competing financial interest.

■ ACKNOWLEDGMENTS

This work was supported by the National Natural Science Foundation of China (no. 22076089) and the Natural Science Foundation of Shandong Province (no. ZR201911070516).

■ REFERENCES

(1) Chen, L.; Zhang, X.; Cao, M.; Pan, Y.; Xiao, C.; Wang, P.; Liang, Y.; Liu, G.; Cai, Y. *Chemosphere* **2021**, *275*, 130011.
(2) Végh, R.; Csóka, M.; Sörös, C.; Sipos, L. *Trends Food Sci. Technol.* **2021**, *114*, 490−509.
(3) Liu, H.; Wang, J.; Jin, H.; Wei, M.; Ren, W.; Zhang, Y.; Wu, L.; He, B. *Sens. Actuators, B* **2021**, *329*, 129215.
(4) Dey, D. K.; Chang, S. N.; Kang, S. C. *Environ. Pollut.* **2021**, *268*, 115713.
(5) Hu, Z.; Lustig, W. P.; Zhang, J.; Zheng, C.; Wang, H.; Teat, S. J.; Gong, Q.; Rudd, N. D.; Li, J. *J. Am. Chem. Soc.* **2015**, *137*, 16209−16215.
(6) Borowska, M.; Jankowski, K. *Talanta* **2020**, *219*, 121162.
(7) Zhang, S.; Zhang, D.; Zhang, X.; Shang, D.; Xue, Z.; Shan, D.; Lu, X. *Anal. Chem.* **2017**, *89*, 3538−3544.
(8) Zhu, Y.; Xu, Y.; Yang, Q. *J. Hazard. Mater.* **2021**, *414*, 125569.
(9) Wu, L.; Zhou, M.; Wang, Y.; Liu, J. *J. Hazard. Mater.* **2020**, *399*, 123154.
(10) Xu, Z.; Long, L.-l.; Chen, Y.-q.; Chen, M.-L.; Cheng, Y.-H. *Food Chem.* **2021**, *338*, 128039.
(11) Li, H.; Du, H.; Wu, D.; Jie, G. *Sens. Actuators, B* **2021**, *345*, 130426.
(12) Chang, J.; Lv, W.; Wu, J.; Li, H.; Li, F. *Chin. Chem. Lett.* **2021**, *32*, 775−778.
(13) He, W.; Qiao, B.; Li, F.; Pan, L.; Chen, D.; Cao, Y.; Tu, J.; Wang, X.; Lv, C.; Wu, Q. *Chem. Commun.* **2021**, *57*, 619−622.
(14) Shen, K.; Chen, X.; Chen, J.; Li, Y. *ACS Catal.* **2016**, *6*, 5887−5903.
(15) Ling, P.; Lei, J.; Ju, H. *Anal. Chem.* **2016**, *88*, 10680−10686.
(16) Yang, R.; Yan, X.; Li, Y.; Zhang, X.; Chen, J. *ACS Appl. Mater. Interfaces* **2017**, *9*, 42482−42491.
(17) Zhang, Y.; Ma, Q.; Yan, Y.; Guo, C.; Xu, S.; Wang, L. *Anal. Chem.* **2020**, *92*, 15679−15684.
(18) Fu, Y.; Xiao, K.; Zhang, X.; Du, C.; Chen, J. *Anal. Chem.* **2021**, *93*, 1076−1083.
(19) Liu, S.; Jia, Y.; Li, Y.; Wang, P.; Xu, Z.; Liu, Q.; Li, Y.; Wei, Q. *ACS Sens.* **2020**, *5*, 3540−3546.
(20) Chen, X.; Liu, Y.; Xu, L.; Wang, Y.; Li, R.; Sun, P.; Lin, Z.; Yang, H. *Anal. Chem.* **2019**, *91*, 13712−13719.
(21) Ouyang, C.; Zhang, S.; Xue, C.; Yu, X.; Xu, H.; Wang, Z.; Lu, Y.; Wu, Z.-S. *J. Am. Chem. Soc.* **2020**, *142*, 1265−1277.
(22) Cai, Q.; Wu, D.; Li, H.; Jie, G.; Zhou, H. *Biosens. Bioelectron.* **2021**, *191*, 113455.
(23) Wu, L.; Chen, K.; Lu, Z.; Li, T.; Shao, K.; Shao, F.; Han, H. *Anal. Chim. Acta* **2014**, *845*, 92−97.
(24) Yang, R.; Yan, X.; Li, Y.; Zhang, X.; Chen, J. *ACS Appl. Mater. Interfaces* **2017**, *9*, 42482−42491.
(25) Shi, X.-M.; Fan, G.-C.; Shen, Q.; Zhu, J.-J. *ACS Appl. Mater. Interfaces* **2016**, *8*, 35091−35098.
(26) Chen, W.; Zhang, X.; Ai, F.; Yang, X.; Zhu, G.; Wang, F. *Inorg. Chem.* **2016**, *55*, 5750−5752.
(27) Guo, X.; Li, L.; Zhang, X.; Chen, J. *Chemelectrochem* **2015**, *2*, 404−411.
(28) Lu, Y.; Zhao, H.; Fan, G.-C.; Luo, X. *Biosens. Bioelectron.* **2019**, *142*, 111569.
(29) Li, B.; Zhang, C.; Jiang, B.; Han, W.; Lin, Z. *Angew. Chem., Int. Ed.* **2015**, *54*, 4250.
(30) Shimron, S.; Wang, F.; Orbach, R.; Willner, I. *Anal. Chem.* **2012**, *84*, 1042−1048.
(31) Wang, W.; Gao, Y.; Wang, W.; Zhang, J.; Li, Q.; Wu, Z.-S. *Anal. Chem.* **2022**, *94*, 1029−1036.
(32) Li, C.; Li, H.; Jie, G. *Microchim. Acta* **2020**, *187*, 625.

(33) Gao, X.; Niu, S.; Ge, J.; Luan, Q.; Jie, G. *Biosens. Bioelectron.* **2020**, *147*, 111778.

https://doi.org/10.1021/acs.analchem.1c05250
Anal. Chem. 2022, 94, 5814−5822